2:1 Spatial Resonance in Langmuir Circulation

Bevin Maultsby

University of North Carolina

Langmuir circulation in the upper layer of the ocean is studied as $2:1$ spatial resonance problem with steady state-steady state modal interaction and $O(2)$ symmetry. A center manifold reduction using asymptotic analysis results in a dynamical system with a structurally stable and attracting heteroclinic orbit in an invariant subspace of the center manifold. This heteroclinic orbit is used to illustrate the persistent switching between a two-roll state and a four-roll state in the crosswind plane. Lastly, a set of coupled PDEs are derived to study the Y junctions which mark transitions between these two states.

1 Introduction

Langmuir circulation is a wind- and surface wave-driven convective process in the upper layer of bodies of water. When the speed of the wind over the surface of the water exceeds approximately 3.5 meters per second, it can create pairs of counter rotating vortices with axis parallel to the wind and the direction of wave propagation, see Figure 1. The rotation of these vortices creates a mixing layer, which in the ocean typically ranges from 50 meters to 100 meters deep.

The counter rotation cause regions of upwelling and strong downwelling in the mixing layer. The downwelling, caused when water converges on the surface and is forced downward, may trap dirt and debris, resulting in a visible pattern of "windrows" on the surface of the water. The windrows are not perfectly parallel, however, and often display "Y junctions" where two windrows appear to merge into one windrow, as seen in Figure 1. These Y junctions can point in either direction, but most often the stem of the Y is observed pointing in the direction of the wind.

Suppose there is a box in the cross-wind plane of width W with periodic sidewalls. When there is a single pair of counter-rotating vortices within this box, this will be referred to as a 2-roll state; when there are two pairs of vortices, it is a 4-roll state. A direct numerical simulation in such a box of the governing equations carried about by Zhexuan Zhang at the University of New Hampshire showed a persistent switching between a 4-roll state, to a 2-roll state, and then back to the 4-roll state with a shift by $W/4$. In this project, we are interested in finding a dynamical systems explanation for this switching behavior between two rolls and four rolls using a pair of coupled ODEs. Then we derive a pair of coupled PDEs to study the Lagrangian pattern of Y junctions on the surface.

The rest of this paper is organized as follows. The equations for the fluid motion are given in Section 2. In Section 3, evolution equations describing how the amplitudes of the

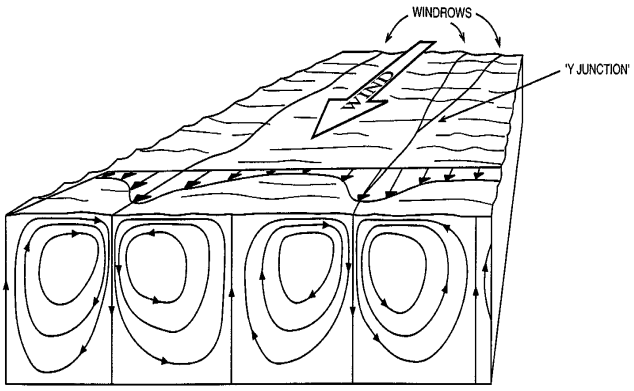

Figure 1: Two pairs of counter-rotating rolls in Langmuir circulation. Note the axes of the rolls is parallel to the direction of the wind. The downwelling between the rolls creates windrows seen on the surface. Where two windrows appear to merge, they form a Y junction. From [15].

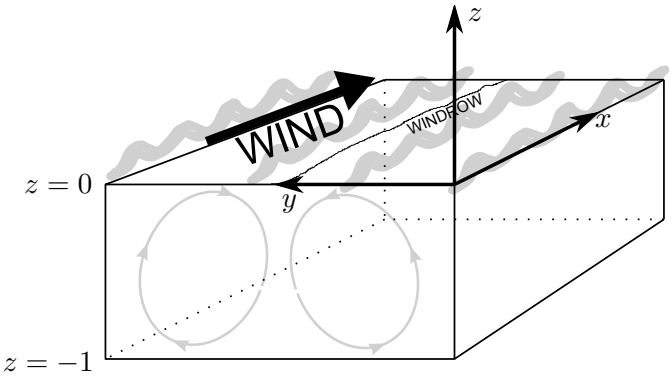

Figure 2: This figure illustrates the spatial coordinate system: x is in the direction of the wind, y is the lateral coordinate in the crosswind plane, and z is the vertical depth (after rescaling, the depth of the water is 1). Note the velocity u is in the x-direction, v is in the y-direction, and w is in the z-direction. Under the coordinate change $(u, v, w) \to (u, \Omega, \psi)$, u remains the velocity in the x-direction, ψ is the streamfunction in the (y, z)-plane, and Ω is the vorticity.

2-roll state and the 4-roll state vary with time are derived using asymptotic analysis. The dynamics of the resulting ODEs are explored. Lastly, in Section 4, slow advection in the downstream direction is added to the system, yielding a set a reduced 3D equations. These equations add terms to the derived ODEs to convert them into PDEs.

2 The governing equations

Let u be the velocity in the direction of the wind, which we will consider the x-direction. Let v be the velocity in the direction perpendicular to the wind, the y-direction, and let w be the velocity in the vertical z-direction (i.e. z measures the depth of the water). See Figure 2.

The basic flow in the x-direction is a linear Couette flow denoted $U_B(z)$; this state carries the wind stress, so the perturbation to the basic state is zero. Thus the overall velocity in this direction is the sum of $U_B(z)$ and a perturbation term u_p. There is no assumed basic flow in the y- or z-directions, hence the only velocity components in the plane perpendicular to the wind arise from the perturbation. Therefore the terms v and w denote the perturbation terms in the y- and z-directions.

Restricting attention to the (y, z)-plane, there are two symmetries; both can be observed in Figure 1. Once a z-axis is chosen so that it passes between a pair of rolls as in Figure 2, there is a reflection action ζ that changes the (v, w)-velocity components via

$$v(y, z) \rightarrow -v(-y, z), \tag{1}$$
$$w(y, z) \rightarrow w(-y, z), \tag{2}$$

which is an action of $\mathbb{Z}/2\mathbb{Z}$ on (v, w). The second symmetry stems from translation, $y \rightarrow y+d$ mod W, where W is the spatial period of y. This is an action of $SO(2)$ on the system. Hence there is overall a group action of $O(2) = SO(2) \rtimes \mathbb{Z}/2\mathbb{Z}$ in the (y, z)-plane.

Let $U = (u, v, w)$. The governing PDE is Navier-Stokes with a Craik-Leibovich forcing term. Craik-Leibovich equations are a surface-wave filtered version of Navier-Stokes in which the average effects of the surface waves show up in a vortex force term, see [8]. The PDE, whose terms will be defined below, is

$$\partial_t U + U \cdot \nabla U = -\nabla p + \frac{1}{La_t^2} \left[U_s(z)\hat{e}_x \times \omega\right] + \frac{1}{Re_*}\nabla^2 U. \tag{3}$$

In (3) U is incompressible, so $\nabla \cdot U = 0$, and $\omega = \nabla \times U$ is vorticity. The nondimensional friction Reynolds number Re_* is defined as

$$Re_* := \frac{u_* H}{\nu_e}, \tag{4}$$

where u_* is a given surface friction velocity, often about $0.01\frac{\mathrm{m}}{\mathrm{s}}$, H is the depth of the mixed layer, and ν_e is a given eddy viscosity that arises as a result of the time averaging. The Craik-Leibovich term in (3) is

$$\frac{1}{La_t^2} \left[U_s(z)\hat{e}_x \times \omega\right]. \tag{5}$$

The function $U_s(z)$ is the Stokes drift. This is a Lagrangian time-averaged velocity following a particle in the surface wave field; it measures the horizontal displacement in the direction of the wind (the $\hat{e}_x$-direction) as a function of depth z in the water. To simplify the analysis, it can be taken to be linear; to be more realistic, however, we use an exponential profile:

$$U_s(z) = U_{s_0} e^{2\beta z}, \tag{6}$$

where U_{s_0} is the horizontal displacement in the direction of wave propagation at the surface. The number $\beta > 0$ is an inverse scale height of the Stokes drift and will be treated as a parameter. The Craik-Leibovich computation includes a wind stress term given by

$$\tau_w \equiv \rho_w u_*^2, \tag{7}$$

where ρ_w is the density of the water.

In (5), La_t is the "turbulent Langmuir number,"

$$La_t = \sqrt{\frac{u_*}{U_{s_0}}}, \tag{8}$$

which is a measure of the strength of the wind driving compared to the wave driving. As a typical value of U_{s_0} is $0.1\frac{\mathrm{m}}{\mathrm{s}}$, a typical value for La_t is around 0.3.

Craik and Leibovich derived this theory using multiple time scale asymptotics with a fast time scale for the waves and a slower time scale for the Langmuir currents. Although (3) is already nondimensional, in section 2.1 we rescale the system. Note that we assume there is no Coriolis force, nor any stratification in the fluid.

2.1 Rescaled Equations

For the remainder of Section 1 up to Section 4, we will work in a "2-dimensional, 3 component" (2D/3C) setting. In other words, there are three velocity components (u, v, w) which depend solely on the two spatial coordinates y and z. The 2D/3C assumption is a reasonable one as Langmuir circulation is highly anistropic; long parallel windrows in the x-direction can be observed on a long scale compared to the scale of the rolls in the crosswind (y, z)-plane.

One of the important consequences of this assumption is that we can rescale the terms in (3) to replace the two parameters La_t and Re_* by the "laminar Langmuir number,"

$$La = \frac{\nu_e}{\sqrt{(u_* Re_*) u_{s_0}} H}, \tag{9}$$

which is a single parameter for the analysis in Section 3. The laminar Langmuir number includes forcing from both the wind and the waves and is typically about ten times smaller than the turbulent Langmuir number. The term $u_* Re_*$ in the denominator is used to scale the flow in the x-direction to make it non-dimensional. The basic flow from the wind in this direction is given by

$$U_B(z) = u_* Re_* \frac{z}{H} + u_0. \tag{10}$$

Here u_* and u_0 have dimensions of speed, Re_* and $\frac{z}{H}$ are dimensionless, thus U_B has units of speed. We scale z so that the depth H of the mixed layer is 1; then after nondimensionalization, the wind stress conditions ends up being

$$\partial_z U_B(z) = 1; \tag{11}$$

we also scale $U_B(z)$ so that $u_0 = 1$. The directional velocities in the y- and z-directions are rescaled differently, using

$$\sqrt{(u_* Re_*) u_{s_0}}. \tag{12}$$

Notice that as Re_* is dimensionless and u_* and u_{s_0} are speeds, the above has a unit of $\frac{\mathrm{m}}{\mathrm{s}}$.

2.2 Coordinate equations

The assumption that U is incompressible together with the 2D/3C requirement that $\frac{\partial}{\partial x}(\cdot) = 0$ yields a natural definition of a streamfunction ψ, defined up to a constant by

$$\partial_z \psi := v, \qquad -\partial_y \psi := w. \tag{13}$$

The vorticity Ω is defined by

$$\Omega = -\nabla^2 \psi. \tag{14}$$

We can rewrite the nondimensionalized version of (3) in component form using the fields u, Ω, ψ rather than the directional velocities u, v, w. This form of the equations is obtained by computing the curl of Craik-Leibovich and then taking the inner product of the result with x; this computation removes the pressure term from the resulting equations. More simply, as there is no x-dependence, it suffices to cross-differentiate the v and w component equations to get an equation for Ω.

Setting $J(\cdot, \cdot)$ be the Jacobian

$$J(f, g) = \frac{\partial f}{\partial y}\frac{\partial g}{\partial z} - \frac{\partial f}{\partial z}\frac{\partial g}{\partial y},$$

the resulting system of equations can be written in component form as

$$\partial_t u + J(u_p, \psi) - \partial_y \psi \frac{dU_B}{dz} = La \nabla^2 u, \tag{15}$$

$$\partial_t \Omega + J(\Omega, \psi) = -\frac{dU_s}{dz}\partial_y u + La \nabla^2 \Omega, \tag{16}$$

$$\nabla^2 \psi = -\Omega. \tag{17}$$

Notice that with the nondimensionalization, $U_B(z) = z + 1$; (15) therefore simplifies to

$$\partial_t u + J(u_p, \psi) - \partial_y \psi = La \nabla^2 u.$$

2.3 Boundary Conditions

At this point there has been no mention of the boundary conditions for u, Ω and ψ. As the sidewalls of our box are periodic, the fields are correspondingly periodic in y. As is common in air-wind interface, we use shear stress-free conditions, thus $\partial_z v = 0$. Furthermore, $w = 0$ at $z = 0$ due to the Craik-Leibovich filtered term: the surface waves have been averaged out so that there is no vertical displacement at the top. As $w = 0$ and $w = -\partial_y \psi$, the streamfunction does not change with y. As ψ is defined up to a constant, we set

$$\psi = 0 \tag{18}$$

at the top. Moreover, notice

$$\Omega = \partial_y w - \partial_z v = 0. \tag{19}$$

Similarly, at $z = -1$, there is no normal flow, and we assume the same conditions for ψ and Ω at the bottom of the mixed layer $z = -1$.

The conditions on the downstream velocity u are chosen with several points in mind. In particular, the bottom boundary is not a true physical boundary; this is especially true for the deep ocean, where beneath the mixing layer is water whose depth may be considered virtually infinite. At the surface, it is natural to impose a fixed stress condition between the air and water; after rescaling, the boundary condition for u at the top is

$$\partial_z u = 1, \tag{20}$$

implying that $\partial_z u_p = 0$.

The bottom boundary condition on u is chosen not only to reflect the physics of the circulation, but also in way that allows for $2:1$ spatial resonance theory to be used in our analysis. As the parameter La is inversely proportional to the Reynolds number, then for a fixed wavenumber k, decreasing La (equivalently increasing La^{-1}) has the effect of increased forcing on the system. At some critical value of La, a mode with wavenumber k bifurcates from a stable state to an unstable state. In numerical simulations of (3) with fixed-stress boundary conditions, as the forcing on the system is increased, the first mode to go unstable is $k = 0$. Physically this mode represents one long flat convection cell with an infinitely long wavelength. The preference for these long scales at onset is a consequence of taking the same stress at the bottom of the layer as at the top.

If the first mode to change stability is the physically unrealistic $k = 0$ mode, then no $2:1$ spatial resonance can be observed from weakly nonlinear theory. Thus in the following calculations, we will use a mixed boundary condition, also known as a Robin boundary condition, at $z = -1$. This condition is physically realistic because though the wind stress is assumed to be fixed, the water in the mixed layer may move at a faster speed than the water below; at the very least, there will be some viscous stress at the bottom layer. The mixed boundary conditions are beneficial as they indicate that the stress is proportional to a difference in speeds in the downstream direction.

The resulting condition

$$\partial_z u - \gamma u = 0 \tag{21}$$

applies to the perturbation u_p, as $U_B(-1) \equiv 0$. The parameter γ is a small, positive constant often referred to as a Biot number. It is discussed in greater detail by Cox and Leibovich

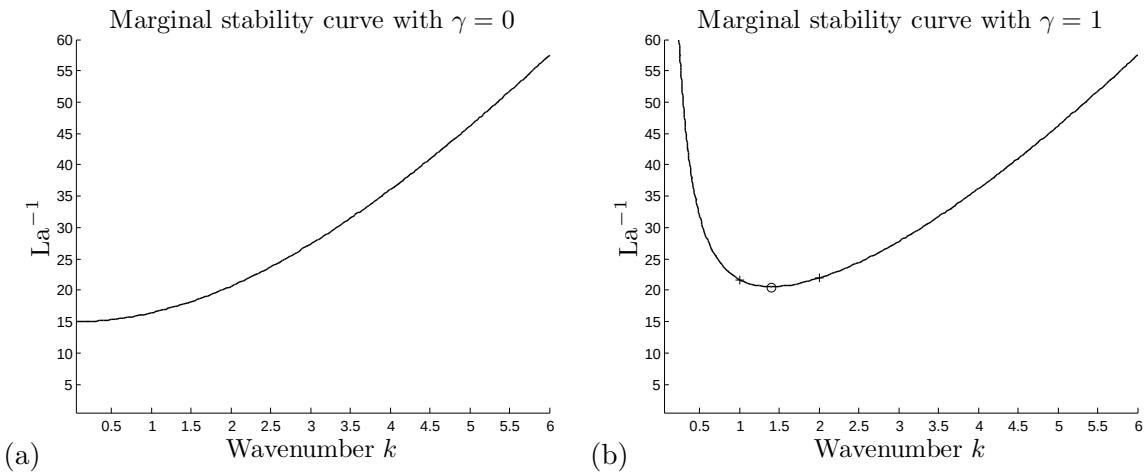

Figure 3: Marginal stability curves for two different sets of boundary conditions. Below each curve the real parts of all eigenvalues are negative, and the system is stable; above the curve there is at least one eigenvalue with positive real part, and the system is unstable. The boundary conditions are identical to those described in Section 2.3 with the exception of the boundary condition on u at $z = -1$. For (a), the bottom boundary condition is $\partial_z u = 0$, while for (b) the bottom boundary condition is $\partial_z u - \gamma u = 0$. As a result of the mixed conditions in (b), the first mode to change stability is no longer at $k = 0$. The two $+$'s indicate the wavenumbers k_0 and $2k_0$ which change stability at the same La_0. The $\circ$ marks the wavenumber where the initial onset of instability occurs. The Stokes drift is $U_s(z) = e^{2(4)z}$, and 30 Chebyshev grid points were used.

(c.f. [5], [6], [7]). This stipulation has the added benefit of altering which modes undergo an initial change in stability as La is decreased; in particular $k = 0$ is no longer the first mode to go unstable. See Figure 3 for a comparison between the marginal stability curve with fixed-stress boundary conditions and with mixed boundary conditions.

3 Evolution Equations

It is possible that for some value of La, two modes undergo simultaneous bifurcation; as this arises from varying not only La but also k, this is a codimension-2 bifurcation. The terminology "$m : n$ spatial resonance" refers to a situation in which two separate modes with spatial ratio is $m : n$ experience such a bifurcation. Of interest here is the case $m = 2$, $n = 1$, which corresponds to wavenumbers k_0 and $2k_0$ changing stability at the same Langmuir number, which we will denote La_0.

In this section, we construct equations for the fields u, ψ and Ω in terms of the modes k_0 and $2k_0$. Each mode will contain an amplitude term: $A(t)$ for the k_0 mode, also referred to as the "single mode," and $B(t)$ for the $2k_0$ mode, the "double mode," where t is time. These equations describe how the two modes are activated at a particular instant; for example, if $A(T) = 0$ for some time T, then only the $2k_0$ mode is activated, and a 4-roll state is observed at time T.

To illustrate the persistent switching between 4 rolls and 2 rolls in a box of width $2\pi/k_0$, we derive evolution equations $\dot{A} = f_1(A, B)$ and $\dot{B} = f_2(A, B)$. These equations must commute with the representation of $O(2)$ given by

$$\vartheta \cdot (A, B) = (e^{i\vartheta}A, e^{2i\vartheta}B), \tag{22}$$

$$\zeta \cdot (A, B) = (\bar{A}, \bar{B}), \tag{23}$$

where the reflection ζ is defined with respect to a chosen origin in y. A dynamical system that commutes with a group action is referred to as an equivariant dynamical system.

A fixed point (A_0, B_0) of a dynamical system occurs when $\dot{A}$ and $\dot{B}$ evaluated at (A_0, B_0) are both zero. A heteroclinic orbit is a trajectory $\varphi(t)$ in phase space that "connects" two such fixed points (A_0, B_0) and (A_1, B_1) in the sense that

$$\varphi(t) \to (A_0, B_0) \text{ and } \varphi(-t) \to (A_1, B_1) \text{ as } t \to \infty.$$

In other words, the heteroclinic orbit lies in the stable manifold of (A_0, B_0) and the unstable manifold of (A_1, B_1).

In general, heteroclinic orbits are not structurally stable: a heteroclinic orbit is likely to break into two trajectories as parameters in a system are varied. Dynamical systems exhibiting symmetry properties such as the system under consideration here, however, may yield structurally stable heteroclinic orbits. These cycles, found on the center manifold tangent to the center eigenspace, are robust and persist under a range of parameter values.

There are three codimension-2 mode interactions depending on the type of bifurcation occuring at the two points, see [10] for an overview. As the eigenvalues at the bifurcation points are both zero (with zero imaginary part), of interest here is the steady state/state state case, for which the center manifold is 4-dimensional. Thus $(A, B) \in \mathbb{C}^2$.

Using center manifold reduction we derive the amplitude equations for A and B. As shown in [1] and [13], the normal form for such evolution equations up to cubic order is

$$\dot{A} = \mu_1 A + c_{12}\overline{A}B + d_{11}|A|^2 A + d_{12}|B|^2 A, \tag{24}$$
$$\dot{B} = \mu_2 B + c_{11}A^2 + d_{21}|A|^2 B + d_{22}|B|^2 B. \tag{25}$$

where $\cdot = \frac{d}{dt}$. With numerically computed coefficients for these equations, we analyze the resulting dynamics, with particular attention given to the existence of structurally stable heteroclinic orbits.

In addition to the A and B modes in the crosswind plane, the nonlinear terms in (15)-(17) generate an additional mode C for the downstream direction. This is the horizontal mean term with wavenumber zero and will produce a third evolution equation. While A and B have no dependence on C, the evolution equation for C is of the form

$$\dot{C} = \gamma_0 C + \gamma_1|A(\tau_1)|^2 + \gamma_2|B(\tau_1)|^2, \tag{26}$$

where $\cdot = \frac{d}{dt}$ and $\tau_1 = \varepsilon t$; the small parameter $\varepsilon > 0$ is described in Section 3.2. In general, if we suppose the Langmuir cells are very strong, then the horizontally averaged downwind velocity is homogeneous except at the top and bottom of the box. The C mode equation (26) computes the tendency to homogenize the horizontal mean velocity.

3.1 Linear Stability Analysis

We first linearize (15)-(17) about the basic flow $U = (U_B(z), 0, 0)$ with $U_B(z) = z + 1$ and obtain

$$\partial_t u - \partial_y \psi = La\nabla^2 u, \tag{27}$$
$$\partial_t \Omega = -\frac{dU_s}{dz}\partial_y u + La\nabla^2\Omega, \tag{28}$$
$$\nabla^2\psi = -\Omega. \tag{29}$$

In the above, La is a parameter and not the fixed quantity La_0. The boundary conditions do not change with the linearization, as they are already linear (and in fact homogeneous). Using the periodicity of y, we make a normal mode ansatz

$$\begin{pmatrix} u(y,z,t) \\ \Omega(y,z,t) \\ \psi(y,z,t) \end{pmatrix} = \begin{pmatrix} \hat{u}(z) \\ \hat{\Omega}(z) \\ \hat{\psi}(z) \end{pmatrix} e^{iky} e^{\sigma t} + \text{c.c.} \tag{30}$$

where σ is the growth rate, k is an unspecified wavenumber in the lateral direction, and the functions $\hat{u}(z), \hat{\Omega}(z), \hat{\psi}(z)$ are the coordinates of the unknown vertical structure of the flow. With this ansatz, (27)-(29) becomes an ordinary differential eigenvalue problem for σ:

$$\begin{pmatrix} La(D^2-k^2) & 0 & ik \\ -\frac{dU_s}{dz}ik & La(D^2-k^2) & 0 \\ 0 & 1 & D^2-k^2 \end{pmatrix} \begin{pmatrix} \hat{u} \\ \hat{\Omega} \\ \hat{\psi} \end{pmatrix} = \sigma \begin{pmatrix} 1 & 0 & 0 \\ 0 & 1 & 0 \\ 0 & 0 & 0 \end{pmatrix} \begin{pmatrix} \hat{u} \\ \hat{\Omega} \\ \hat{\psi} \end{pmatrix}, \tag{31}$$

where $D = \frac{\partial}{\partial z}$. We discretize the z-direction with 30 Chebyshev points and use Chebyshev spectral methods in Matlab[1] to solve this eigenvalue problem as a two-point boundary value problem in z. For each k in a chosen interval, we find the Langmuir number at which point the stability of the system changes. The result is a marginal stability curve, an example of which can be seen in Figure 3(b).

We locate on this curve the wavenumbers k_0 and $2k_0$ which change stability at essentially the same La_0, and correspondingly set the width of the box in the (y, z)-plane to be $W = \frac{2\pi}{k_0}$. Henceforth, the terms k_0, $2k_0$ and La_0 refer to the quantities found by this eigenvalue calculation.

For the zero-mode equation with amplitude C, we repeat (31) with $k = 0$ and solve

$$\begin{pmatrix} La_0 D^2 & 0 & 0 \\ 0 & La_0 D^2 & 0 \\ 0 & 1 & D^2 \end{pmatrix} \begin{pmatrix} \hat{u}_0 \\ \hat{\Omega}_0 \\ \hat{\psi}_0 \end{pmatrix} = \sigma \begin{pmatrix} 1 & 0 & 0 \\ 0 & 1 & 0 \\ 0 & 0 & 0 \end{pmatrix} \begin{pmatrix} \hat{u}_0 \\ \hat{\Omega}_0 \\ \hat{\psi}_0 \end{pmatrix}. \tag{32}$$

With the chosen boundary conditions, $\hat{\Omega}_0 = \hat{\psi}_0 = 0$. Then (32) reduces to

$$\frac{\partial}{\partial t}\hat{u}_0(z,t) = La_0 \frac{\partial^2}{\partial z^2}\hat{u}_0(z,t). \tag{33}$$

Writing $\hat{u}_0(z,t)$ as

$$\hat{u}_0(z,t) = C(t)\tilde{u}(z), \tag{34}$$

then C satisfies

$$\frac{dC}{dt} = \sigma C(t). \tag{35}$$

Thus γ_0 in (26) is the eigenvalue σ, which is determined numerically. As $k = 0$ is in the stable regime, $\gamma_0 < 0$.

3.2 Weakly nonlinear analysis

Let $\varepsilon > 0$ be a small parameter. As the shape of the marginal stability curve seen in Figure 3(b) is parabolic near the onset of instability, varying the wavenumber k by ε corresponds to a change in La^{-1} by ε^2. In particular, since we want small amplitude perturbations just above the onset of instability, a small parameter $\mu > 0$ is used to vary the height of the parameter La^{-1} over the marginal stability curve in Figure 3(b). Then La^{-1} can be written

$$La^{-1} = La_0^{-1} + \mu\varepsilon^2. \tag{36}$$

The role of the small parameter μ will be made more precise in Section 3.4. As we are interested in a weakly nonlinear regime, the small perturbation terms added to each field are $O(\varepsilon)$, and each field can be expanded in powers of ε in the following way:

$$u = U_B + \varepsilon u_1 + \varepsilon^2 u_2 + \cdots, \tag{37}$$

$$\Omega = \varepsilon\Omega_1 + \varepsilon^2\Omega_2 + \cdots, \tag{38}$$

$$\psi = \varepsilon\psi_1 + \varepsilon^2\psi_2 + \cdots. \tag{39}$$

[1]Based on methods and code in [16].

Lastly, we introduce slow times $\tau_1 = \varepsilon t$ and $\tau_2 = \varepsilon^2 t$ so that

$$\frac{\partial}{\partial t} = \varepsilon \frac{\partial}{\partial \tau_1} + \varepsilon^2 \frac{\partial}{\partial \tau_2}. \tag{40}$$

This separation of time scales will cause the quadratic terms $\overline{A}B$ and A^2 of the evolution equation in (24)-(25) to emerge in the analysis at $O(\varepsilon^2)$, while the rest of the terms will emerge at $O(\varepsilon^3)$. Substituting the terms obtained at each step into (40) yields evolution equations of the form

$$\begin{aligned} \dot{A} &= \varepsilon^2 \mu_1 A + \varepsilon c_{12} \overline{A} B + \varepsilon^2 e_{11} |A|^2 A + \varepsilon^2 e_{12} |B|^2 A, & (41) \\ \dot{B} &= \varepsilon^2 \mu_2 B + \varepsilon c_{11} A^2 + \varepsilon^2 e_{21} |A|^2 B + \varepsilon^2 e_{22} |B|^2 B, & (42) \end{aligned}$$

where $\cdot = \frac{\partial}{\partial t}$. After multipling both sides of the above by ε and rescaling via

$$\varepsilon A \to A, \qquad \varepsilon B \to B, \qquad \varepsilon^2 \mu_i \to \mu_i,$$

the equations have the expected form

$$\begin{aligned} \dot{A} &= \mu_1 A + c_{12} \overline{A} B + e_{11} |A|^2 A + e_{12} |B|^2 A, & (43) \\ \dot{B} &= \mu_2 B + c_{11} A^2 + e_{21} |A|^2 B + e_{22} |B|^2 B & (44) \end{aligned}$$

where μ_i is $O(\varepsilon^2)$, A and B are $O(\varepsilon)$, while c_{1i} and e_{ij} are $O(1)$. For amplitude C of the zero-mode equation, the coefficient γ_0 emerges from the linear stability analysis, while γ_1 and γ_2 are found at $O(\varepsilon^2)$ with the slow time scale τ_1. Hence C is $O(\varepsilon^2)$.

The leading $O(\varepsilon)$ terms are written

$$\begin{aligned} u_1(y, z, \tau_1) &= A(\tau_1) e^{ik_0 y} u_{11}(z) + B(\tau_1) e^{2ik_0 y} u_{12}(z) + \text{c.c.}, & (45) \\ \Omega_1(y, z, \tau_1) &= A(\tau_1) e^{ik_0 y} \Omega_{11}(z) + B(\tau_1) e^{2ik_0 y} \Omega_{12}(z) + \text{c.c.}, & (46) \\ \psi_1(y, z, \tau_1) &= A(\tau_1) e^{ik_0 y} \psi_{11}(z) + B(\tau_1) e^{2ik_0 y} \psi_{12}(z) + \text{c.c.}, & (47) \end{aligned}$$

where c.c. denotes the complex conjugate, as each field must be real. We solve the $O(\varepsilon)$ system numerically for the functions u_{ij}, Ω_{ij} and ψ_{ij}, $i, j \in \{1, 2\}$ by solving for the eigenvectors of the system (31) with $\sigma = 0$.

The $O(\varepsilon^2)$ terms u_2, Ω_2, ψ_2 are written similarly but inevitably have more wavenumbers due to the mode-mode interaction in the nonlinear terms of (15)-(17). For example, the $e^{ik_0 y}$ and $e^{2ik_0 y}$ modes interact to generate a mode of wavenumber 3; overall, at $O(\varepsilon^2)$ there are 9 total terms corresponding to each of

$$e^0, e^{\pm ik_0 y}, e^{\pm 2ik_0 y}, e^{\pm 3ik_0 y}, e^{\pm 4ik_0 y}.$$

Notice that the wavenumbers 0, 3 and 4 are all in the stable regime as they lie under the marginal stability curve for the fixed value of La.

We remark further that the mode-mode interaction can reinforce the single mode $e^{ik_0 y}$ and the double mode $e^{2ik_0 y}$. The former occurs when $e^{2ik_0 y}$ interacts with $e^{-ik_0 y}$, while the latter occurs when $e^{ik_0 y}$ interacts with itself. Therefore, when the evolution equations for the amplitudes A and B are written in such a way that these modes are only weakly

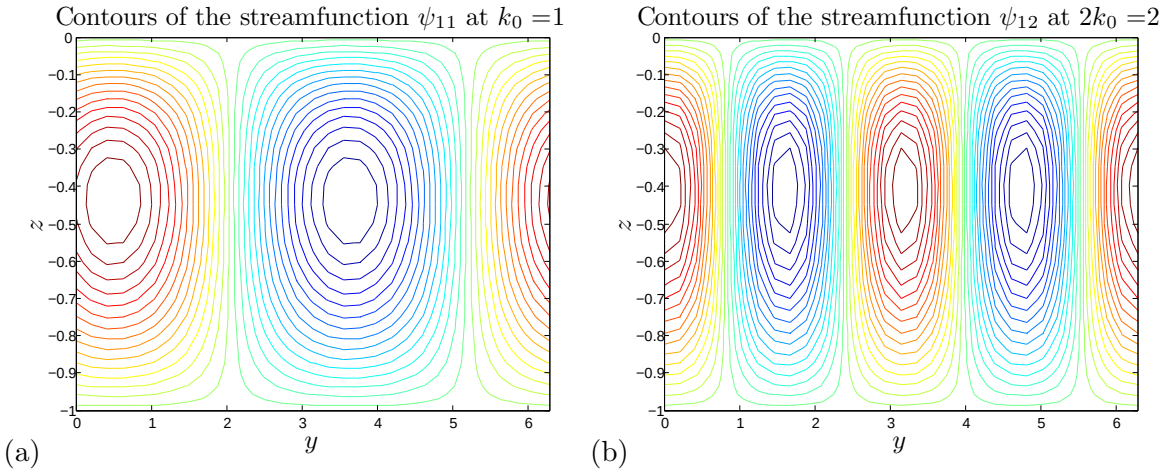

Figure 4: These plots illustrate the Langmuir cells for the (a) 2 roll case and (b) 4 roll case. (a) is obtained by computing $\psi_{11}(z)$ from (47), and then plotting $e^{ik_0y}\psi_{11}(z)$ in the (y,z)-plane with periodic sidewalls. (b) is obtained the same way for $\psi_{12}(z)$ and e^{2ik_0y}. Thirty Chebyshev grid points were used.

growing, the interaction of $\bar{A}$ and B will produce a source term for A, while A and A will produce a source term for B. These evolution equations are thus modified by the $2:1$ resonance. Notice that this observation agrees with the normal form equations (24) and (25).

Lastly, we note that the appearance of wavenumber zero terms at $O(\varepsilon^2)$ yields an equation for the C mode; the mean flow averaged over y can be written

$$\overline{u}(z,\tau_1) = U_B(z) + O(\varepsilon^2) = U_B(z) + \varepsilon^2 \hat{u}_1(z) C(\tau_1), \tag{48}$$

where $\hat{u}_1(z)$ is the vertical structure of the $O(\varepsilon^2)$ term. This equation is consistent with (45) as C is $O(\varepsilon)$ in (45). While the horizontal mean at $O(\varepsilon)$ stage in equations (45)-(47) is zero, the mode-mode interactions e^{ik_0y} with e^{-ik_0y} and e^{2ik_0y} with e^{-2ik_0y} give a nontrivial projection to the horizontal mean. Notice this mode-mode interaction justifies the form of equation (26).

3.2.1 The Fredholm Alternative

Let $\langle \cdot, \cdot \rangle$ be the Hermitian L^2 inner product

$$\langle v_1, v_2 \rangle = \iint_D v_1 \cdot \overline{v_2}\, dy\, dz,$$

where the domain D is the box $[0, 2\pi/k_0] \times [-1, 0]$ in the cross-wind plane, and $\cdot$ denotes the standard Euclidean inner product. Let L be the linear operator

$$L = \begin{pmatrix} La\nabla^2 & 0 & \partial_y \\ 0 & 1 & \nabla^2 \\ -\frac{dU_s}{dz}\partial_y & La\nabla^2 & 0 \end{pmatrix}, \tag{49}$$

and let $L^\dagger$ be its adjoint. By the Fredholm alternative, $L(u,\Omega,\psi)^t = (f,g,h)^t$ has a solution if and only if

$$\Big\langle (u^\dagger,\Omega^\dagger,\psi^\dagger),(f,g,h)\Big\rangle = 0, \tag{50}$$

where $(u^\dagger,\Omega^\dagger,\psi^\dagger)^t$ is in the null space of $L^\dagger$.

L is an operator acting on the space of triples of functions $(u,\Omega,\psi)^t$ with u, Ω and ψ satisfying the boundary conditions in Section 2.3. Suppose (u^*,Ω^*,ψ^*) satisfies identical boundary conditions to (u,Ω,ψ). Let M be the diagonal matrix

$$M = \begin{pmatrix} \frac{dU_s}{dz} & 0 & 0 \\ 0 & La & 0 \\ 0 & 0 & 1 \end{pmatrix}, \tag{51}$$

and set $L_M = ML$. Using integration by parts with the definition of the adjoint,

$$\iint_D (u^*,\Omega^*,\psi^*)\cdot\overline{(L_M(u,\Omega,\psi)^t)^t}\,dy\,dz = \iint_D \left(L_M^\dagger(u^*,\Omega^*,\psi^*)^t\right)^t\cdot\overline{(u,\Omega,\psi)}\,dy\,dz, \tag{52}$$

we determine that L_M is self-adjoint. A simpler calculation also shows that $M^\dagger = M$. Thus

$$ML = (ML)^\dagger = L^\dagger M^\dagger = L^\dagger M,$$

which implies that

$$L^\dagger = MLM^{-1} = \begin{pmatrix} La\nabla^2 & 0 & \frac{dU_s}{dz}\partial_y \\ 0 & 1 & La\nabla^2 \\ -\partial_y & \nabla^2 & 0 \end{pmatrix}. \tag{53}$$

3.2.2 Order ε

Equations (37)-(39) are substituted into (15)-(17). The $O(\varepsilon)$ equations are

$$-La\nabla^2 u_1 - \partial_y\psi_1 = 0, \tag{54}$$

$$-\frac{dU_s}{dz}\partial_y u_1 + La\nabla^2\Omega_1 = 0, \tag{55}$$

$$\Omega_1 + \nabla^2\psi_1 = 0, \tag{56}$$

where u_1,Ω_1,ψ_1 are the functions from (45)-(47). The form of these equations is identical to the linear stability analysis in (27)-(29) with $\frac{\partial}{\partial t} = 0$ as the onset of instability occurs along the marginal stability curve.

There are two separate calculations performed, as ∂_y becomes multiplication by ik_0 when it acts on the single mode and by $2ik_0$ when it acts on the double mode. Solving for eigenvectors $(u_1,\Omega_1,\psi_1)^t$ satisfying

$$L\begin{pmatrix} u_1 \\ \Omega_1 \\ \psi_1 \end{pmatrix} = 0 \tag{57}$$

yields two vectors: $E_1 = (u_{11},\Omega_{11},\psi_{11})^t$ for the single mode structure and $E_2 = (u_{12},\Omega_{12},\psi_{12})^t$ for the double mode. Plots of ψ_{11} and ψ_{12} are seen in Figure 4.

Set $E_{11} = E_1$, $E_{12} = \overline{E_1}$, $E_{21} = E_2$ and $E_{22} = \overline{E_2}$. Then

$$\begin{pmatrix} u_1 \\ \Omega_1 \\ \psi_1 \end{pmatrix} = Ae^{ik_0 y}E_{11} + Be^{2ik_0 y}E_{21} + \overline{A}e^{-ik_0 y}E_{12} + \overline{B}e^{-2ik_0 y}E_{22}.$$

With the same process, we also compute four vectors $E_{ij}^\dagger$ in the kernel of $L^\dagger$ to use in the calculations for the Fredholm alternative in the next two sections.

3.2.3 Order ε^2

After substituting (37)-(39) into (15)-(17), the $O(\varepsilon^2)$ system is

$$\begin{aligned} La_0\nabla^2 u_2 + \partial_y \psi_2 &= \partial_{\tau_1} u_1 + J(u_1, \psi_1), & (58)\\ \Omega_2 + \nabla^2 \psi_2 &= 0, & (59)\\ -\frac{dU_s}{dz}\partial_y u_2 + La_0\nabla^2\Omega_2 &= \partial_{\tau_1}\Omega_1 + J(\Omega_1, \psi_1), & (60) \end{aligned}$$

Notice that we already have expressions for u_1, ψ_1, Ω_1 from the $O(\varepsilon)$ case. This can be written in terms of the linear operator L and including the slow time τ_1 as

$$L\begin{pmatrix} u_2 \\ \Omega_2 \\ \psi_2 \end{pmatrix} = \begin{pmatrix} \partial_{\tau_1} u_1 + J(u_1, \psi_1) \\ 0 \\ \partial_{\tau_1}\Omega_1 + J(\Omega_1, \psi_1) \end{pmatrix}. \quad (61)$$

The right-hand side can be explicitly computed with the eigenvectors u_1, ψ_1, Ω_1 found in Section 3.2.2. For the solvability criterion (50), we set

$$\left\langle E_{ij}^\dagger, \begin{pmatrix} \partial_{\tau_1} u_1 + J(u_1, \psi_1) \\ 0 \\ \partial_{\tau_1}\Omega_1 + J(\Omega_1, \psi_1) \end{pmatrix} \right\rangle = 0, \quad (62)$$

$i, j = 1, 2$. We compute this inner product numerically using quadrature and obtain the coefficients of the quadratic terms $\overline{A}B$ and A^2 in the evolutions equations for A and B, respectively; below is an example calculation for the $\overline{A}B$ coefficient. For the vectors in the nullspace of $L^\dagger$ computed in Section 3.2.2, let $E_{ij}^\dagger(z) = (E_{ij,1}^\dagger(z), E_{ij,2}^\dagger(z), E_{ij,3}^\dagger(z))^t$. Then the solvability criterion yields a condition on the derivatives of A and B, found by computing

$$\begin{aligned} 0 &= \left\langle E_{11}^\dagger(z)e^{-ik_0 y}, \begin{pmatrix} \partial_{\tau_1} u_1(y,z,\tau_1) + J(u_1(y,z,\tau_1), \psi_1(y,z,\tau_1)) \\ 0 \\ \partial_{\tau_1}\Omega_1(y,z,\tau_1) + J(\Omega_1(y,z,\tau_1), \psi_1(y,z,\tau_1)) \end{pmatrix} \right\rangle \\ &= \iint_D \left(E_{11,1}^\dagger(z)e^{-ik_0 y}\overline{(\partial_{\tau_1} u_1(y,z,\tau_1) + J(u_1(y,z,\tau_1), \psi_1(y,z,\tau_1)))} \right) dy\, dz \\ &\quad + \iint_D \left(E_{11,3}^\dagger(z)e^{-ik_0 y}\overline{\partial_{\tau_1}\Omega_1(y,z,\tau_1) + J(\Omega_1(y,z,\tau_1), \psi_1(y,z,\tau_1)))} \right) dy\, dz \end{aligned}$$

After simplification, each term in the above integrand contains an expression of the form $e^{mik_0 y}$. If $m \neq 0$, then

$$\int_0^{2\pi/k_0} e^{mik_0 y}\, dy = 0.$$

Hence the only terms from the $\overline{\partial_{\tau_1}(\cdot) + J(\cdot, \psi_1)}$ expressions which contribute nontrivially to the solvability criterion are those whose y-structure after complex conjugation is $e^{ik_0 y}$. Therefore, the solvability criterion can be explicitly written as

$$\begin{aligned}
0 &= \int_{-1}^{0} \left(E^{\dagger}_{11,1}(z) \cdot \left(A_{\tau_1} u_{11}(z) + 2ik_0 \overline{A} B u_{12}(z) \frac{d\overline{\psi_{11}}}{dz} - ik_0 \overline{A} B \overline{u_{11}}(z) \frac{d\psi_{12}}{dz} \right) \right) dz \\
&\quad - \int_{-1}^{0} \left(E^{\dagger}_{11,1}(z) \cdot \left(2ik_0 \overline{A} B \psi_{12}(z) \frac{d\overline{u_{11}}}{dz} - ik_0 \overline{A} B \overline{\psi_{11}}(z) \frac{du_{12}}{dz} \right) \right) dz \\
&\quad + \int_{-1}^{0} \left(E^{\dagger}_{11,3}(z) \cdot \left(A_{\tau_1} \Omega_{11}(z) + 2ik_0 \overline{A} B \Omega_{12}(z) \frac{d\overline{\psi_{11}}}{dz} - ik_0 \overline{A} B \overline{\Omega_{11}}(z) \frac{d\psi_{12}}{dz} \right) \right) dz \\
&\quad - \int_{-1}^{0} \left(E^{\dagger}_{11,3}(z) \cdot \left(2ik_0 \overline{A} B \psi_{12}(z) \frac{d\overline{\Omega_{11}}}{dz} - ik_0 \overline{A} B \overline{\psi_{11}}(z) \frac{d\Omega_{12}}{dz} \right) \right) dz.
\end{aligned}$$

Thus

$$\begin{aligned}
A_{\tau_1} \int_{-1}^{0} \left(E^{\dagger}_{11,1} u_{11} + E^{\dagger}_{11,3} \Omega_{11} \right) dz &= -ik_0 \overline{A} B \left[\int_{-1}^{0} \left(E^{\dagger}_{11,1} \left(2u_{12} \frac{d\overline{\psi_{11}}}{dz} - \overline{u_{11}} \frac{d\psi_{12}}{dz} \right) \right) dz \right. \\
&\quad + \int_{-1}^{0} \left(E^{\dagger}_{11,1} \cdot \left(2\psi_{12} \frac{d\overline{u_{11}}}{dz} - \overline{\psi_{11}} \frac{du_{12}}{dz} \right) \right) dz \\
&\quad - \int_{-1}^{0} \left(E^{\dagger}_{11,3} \cdot \left(2\Omega_{12} \frac{d\overline{\psi_{11}}}{dz} - \overline{\Omega_{11}} \frac{d\psi_{12}}{dz} \right) \right) dz \\
&\quad \left. + \int_{-1}^{0} \left(E^{\dagger}_{11,3} \cdot \left(2\psi_{12} \frac{d\overline{\Omega_{11}}}{dz} - \overline{\psi_{11}} \frac{d\Omega_{12}}{dz} \right) \right) dz. \right]
\end{aligned}$$

The left and right sides of the above can be computed numerically using quadrature methods from [16], chapter 12. Then each integral results in a scalar value, yielding a simple calculation for the coefficient c_{12} in

$$A_{\tau_1} = c_{12} \overline{A} B.$$

In addition, the particular solution $(u_2, \Omega_2, \psi_2)^t$ to (61) is also found numerically in Matlab using the pseudoinverse of the matrix L.

Lastly, due to the presence of wavenumber zero at $O(\varepsilon^2)$, we compute the equation for the amplitude $C(\tau_1)$ of the mean velocity at this order. As a result of horizontal averaging, no Langmuir cells remain; however, there is a correction term in the streamwise flow that reflects the fact that there were cells present. For the solvability criterion to compute the $O(\varepsilon^2)$ contribution to $\dot{C}$, the zero mode version of (61) is written

$$(LaD^2 - \sigma)\hat{u}_2 = (\varepsilon \partial_{\tau_1} C)\, \hat{u}_1(z) + J(u_1, \psi_1)_0, \tag{63}$$

where $J(u_1, \psi_1)_0$ refers to the terms in $J(u_1, \psi_1)$ which have no y-dependence. These are the terms that arise from nonlinear interaction between $e^{ik_0 y}$ and $e^{-ik_0 y}$, and $e^{2ik_0 y}$ and $e^{-2ik_0 y}$. Then (63) has a solution if and only if

$$\langle \hat{u}_1, (\varepsilon \partial_{\tau_1} C)\, \hat{u}_1 + J(u_1, \psi_1)_0 \rangle = 0, \tag{64}$$

which results in

$$\begin{aligned}(\varepsilon\partial_{\tau_1}C)\int_{-1}^{0}|\hat{u}_1(z)|^2\,dz &= -|A|^2\int_{-1}^{0}\hat{u}_1(z)\left(u_{11}(z)\overline{\psi_{11}}(z)+\overline{u_{11}}(z)\psi_{11}(z)\right)\,dz\\ &\quad -|B|^2\int_{-1}^{0}\hat{u}_1(z)\left(u_{12}(z)\overline{\psi_{12}}(z)+\overline{u_{12}}(z)\psi_{12}(z)\right)\,dz.\end{aligned}$$

These integrals are also computed using quadrature methods and yield the coefficients γ_1 and γ_2 from (26). Then

$$\begin{aligned}\dot{C} &= \sigma C+\varepsilon\partial_{\tau_1}C\\ &= \gamma_0 C+\gamma_1|A|^2+\gamma_2|B|^2.\end{aligned}$$

3.2.4 Order ε^3

The remaining cofficients up to cubic order emerge from the $O(\varepsilon^3)$ system:

$$\begin{aligned}\partial_{\tau_1}u_2+\partial_{\tau_2}u_1+J(u_1,\psi_2)+J(u_2,\psi_1)-\partial_y\psi_3 &= La_0\nabla^2u_3-La_0^2\mu\nabla^2u_1,\\ -\Omega_3 &= \nabla^2\psi_3,\\ \partial_{\tau_1}\Omega_2+\partial_{\tau_2}\Omega_1+J(\Omega_1,\psi_2)+J(\Omega_2,\psi_1) &= -\frac{dU_s}{dz}u_3+La_0\nabla^2\Omega_3-La_0^2\mu\nabla^2\Omega_1.\end{aligned}$$

Written as matrices with the same linear operator L, the system is

$$L\begin{pmatrix}u_3\\ \Omega_3\\ \Psi_3\end{pmatrix}=\begin{pmatrix}\partial_{\tau_1}u_2+\partial_{\tau_2}u_1+J(u_1,\psi_2)+J(u_2,\psi_1)+La_0^2\mu\nabla^2u_1\\ 0\\ \partial_{\tau_1}\Omega_2+\partial_{\tau_2}\Omega_2+J(\Omega_1,\psi_2)+J(\Omega_2,\psi_1)+La_0^2\mu\nabla^2\Omega_1\end{pmatrix}. \tag{65}$$

The right-hand side of (65) is calculated using the results from the previous two sections. As before, we compute the inner product of the right-hand side with the vectors $E_{ij}^{\dagger}$ numerically using quadrature. The result gives us the coefficients μ_i, e_{ij}, $i,j\in\{1,2\}$ from (24) and (25). These equations are described in more detail in Section 3.3.

3.3 The evolution equations

Once the vectors u_i, Ω_i and ψ_i have been computed for $i=\{1,2\}$, we use quadrature methods to solve for the coefficients of the evolution equations. As derived in [1] and [13], the normal form of the equations for A and B up to cubic terms is

$$\dot{A} = \mu_1A+c_{12}\overline{A}B+d_{11}|A|^2A+d_{12}|B|^2A, \tag{66}$$

$$\dot{B} = \mu_2B+c_{11}A^2+d_{21}|A|^2B+d_{22}|B|^2B. \tag{67}$$

The reflection symmetry $(A,B)\to(\overline{A},\overline{B})$ forces the coefficients μ_i, c_{ij}, d_{ij}, $i,j\in\{1,2\}$, to be real. There are, however, no automatic requirements for the signs of these coefficients. As discussed in the literature on such equivariant dynamical systems, see Armbruster, *et al.* [1] and Porter and Knobloch [12], different dynamical behavior emerges with different combinations of signs.

For the general setting of 2 : 1 spatial resonance, it is possible that c_{12} and c_{11} have the same sign. This situation is referred to as the "+ case" in [1], and it does not yield particularly interesting dynamics. In particular, there is no heteroclinic orbit present in the $\mathrm{Im}\,(A) = \mathrm{Im}\,(B) = 0$ plane. The other possibility, that c_{12} and c_{11} have different signs, is referred to in [1] as the "− case" and is more fruitful. For the extensive range of parameter values tested thus far, the evolution equations derived in this work have fallen under this "−" category.

Near the onset of instability, the growth rates μ_1 and μ_2 should be positive. The last sign requirement we make is that e_{11} and e_{22} be negative. This requirement will yield a circle of pure modes discussed in Section 3.4 and seen in Figure 5 and, like the requirement on the quadratic terms, has been satisfied for each set of parameters.

As explored by Chossat in [4], hydrodynamical systems with symmetries often produce evolution equations that fulfill such requirements necessary to exhibit interesting dynamical behavior, such as the class of "−" equations under consideration here. These symmetric systems then yield robust heteroclinic connections in the invariant subspaces of the amplitude equations. Thus hydrodynamics can be rewarding to study from the dynamical systems viewpoint, and it is unsurprising that we find the right type of dynamics in our evolution equations for Langmuir circulation.

As an example of amplitude equations found from the calculations of the previous sections, we derive the following with 30 Chebyshev grid points, $\gamma = 1.5$, and $U_s(z) = e^{2(4z)}$:

$$\dot{A} = 0.0070A - 0.0801\overline{A}B - 0.0758|A|^2A - 0.3867|B|^2A, \tag{68}$$
$$\dot{B} = 0.0152B + 0.0987A^2 - 0.7563|A|^2B - 0.3334|B|^2B, \tag{69}$$

$\cdot = \frac{\partial}{\partial t}\cdot$. Additionally, the evolution equation for the horizontal mean term is

$$\dot{C} = -0.0477C + 0.0188|A|^2 + 0.0252|B|^2.$$

As discussed above, (68) and (69) display the desired signs for the coefficients and can be rescaled from the form (66)-(67) to the form (24)-(25), yielding

$$\dot{A} = \mu_1 A + \overline{A}B - 0.9583|A|^2A - 6.0219|B|^2A, \tag{70}$$
$$\dot{B} = \mu_2 B - A^2 - 9.5573|A|^2B - 5.1909|B|^2B. \tag{71}$$

As $A, B \in \mathbb{C}$, they can be written in terms of their real and imaginary parts as

$$A = x_1 + iy_1 = r_1 e^{i\alpha_1},$$
$$B = x_2 + iy_2 = r_2 e^{i\alpha_2},$$

from which (66) and (67) can be written in Cartesian coordinates as

$$\dot{x}_1 = x_1(\mu_1 + e_{11}(x_1^2 + y_1^2) + e_{12}(x_2^2 + y_2^2)) + x_1x_2 + y_1y_2, \tag{72}$$
$$\dot{y}_1 = y_1(\mu_1 + e_{11}(x_1^2 + y_1^2) + e_{12}(x_2^2 + y_2^2)) + x_1y_2 - y_1x_2, \tag{73}$$
$$\dot{x}_2 = x_2(\mu_2 + e_{21}(x_1^2 + y_1^2) + e_{22}(x_2^2 + y_2^2)) - (x_1^2 - y_1^2), \tag{74}$$
$$\dot{y}_2 = y_2(\mu_2 + e_{21}(x_1^2 + y_1^2) + e_{22}(x_2^2 + y_2^2)) - 2x_1y_1. \tag{75}$$

Following the terminology of [1], we will call any fixed point $\dot{A} = \dot{B} = 0$ with $r_1 = 0$ but $r_2 \neq 0$ a *pure mode*, and a fixed point $\dot{A} = \dot{B} = 0$ with $r_1 \neq 0$, $r_2 \neq 0$ a *mixed mode*.

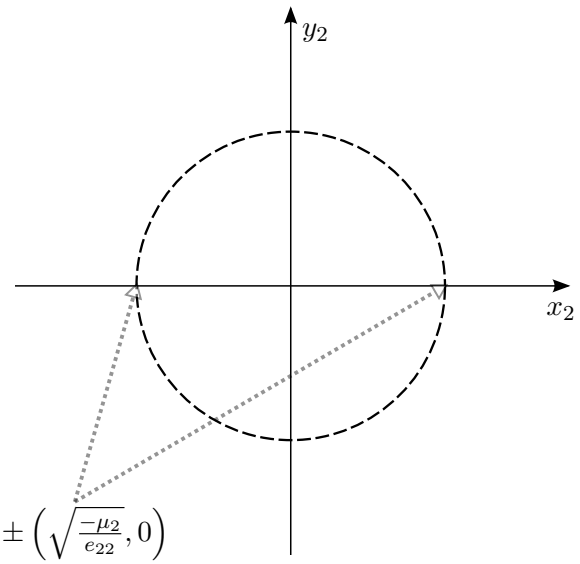

Figure 5: The invariant subspace Σ_1. There is a circle of pure modes given by $|B|^2 = -\frac{\mu_2}{e_{22}}$. The two points where this circle intersects the x_2-axis lie in all three invariant subspaces, as seen in Figure 6.

3.4 Dynamics of the Evolution Equations

As simultaneous bifurcation of modes k_0 and $2k_0$ is a codimension-2 bifurcation problem, two parameters are varied to explore the dynamics. Holding the coefficients μ_1 and μ_2 small and varying them does not effect the other coefficients e_{ij}, $i, j \in \{1, 2\}$. These linear term coefficients can be rewritten as

$$(\mu_1, \mu_2) = \mu(\cos\theta, \sin\theta). \tag{76}$$

Thus μ_1 and μ_2, or equivalently μ and θ, are unfolding parameters; varying μ is equivalent to varying La close to La_0, while varying θ is equivalent to varying the wavenumbers close to k_0 and $2k_0$.

There are three invariant subspaces for $(\dot{A}, \dot{B})$: two 2-dimensional subspaces and their 1-dimensional intersection. The union of the three subspaces can be seen in Figure 6.

1. $\Sigma_1 = \{|A| = 0\}$. On this plane, the flow is given by

$$\dot{A} = 0, \qquad \dot{B} = \mu_2 B + e_{22}|B|^2 B, \tag{77}$$

or equivalently, $\dot{x}_1 = \dot{y}_1 = 0$ and

$$\dot{x}_2 = \mu_2 x_2 + e_{22}(x_2^2 + y_2^2)x_2, \tag{78}$$
$$\dot{y}_2 = \mu_2 y_2 + e_{22}(x_2^2 + y_2^2)y_2. \tag{79}$$

There is a fixed point at the origin; moreover, as $e_{22} < 0$ while $\mu_2 > 0$, every point on the circle $x_2^2 + y_2^2 = -\frac{\mu_2}{e_{22}}$ is a pure mode. Of particular interest are the two pure modes on the x_2 axis,

$$\pm\left(0, 0, \sqrt{\frac{-\mu_2}{e_{22}}}, 0\right), \tag{80}$$

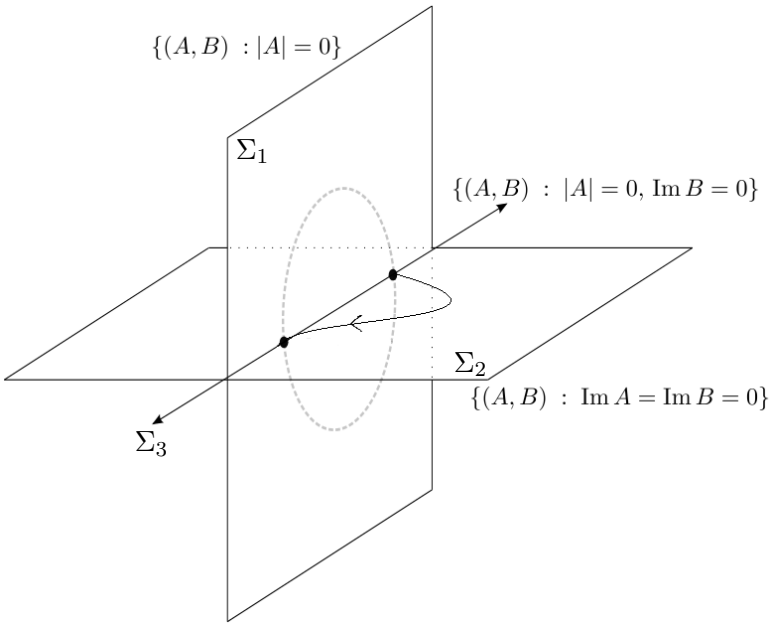

Figure 6: The three invariant subspaces Σ_1-Σ_3. A heteroclinic orbit connecting the two pure modes of (80) is pictured in Σ_2.

seen in Figure 5. These two fixed points appear in Σ_2 below.

2. $\Sigma_2 = \{\mathrm{Im}\, A = \mathrm{Im}\, B = 0\}$. The equations for (72)-(75) become

$$\dot{x}_1 = \mu_1 x_1 + x_1 x_2 + e_{11} x_1^3 + e_{12} x_1 x_2^2, \tag{81}$$
$$\dot{x}_2 = \mu_2 x_2 - x_1^2 + e_{21} x_1^2 x_2 + e_{22} x_2^3, \tag{82}$$

with $\dot{y}_1 = \dot{y}_2 = 0$. The flow in this plane is more complicated that for the previous invariant subspace; however, for any choice of coefficients, the pure modes in (80) are also fixed points of (81) and (82). For certain choices of the coefficients, mixed modes may be present, and there may be a heteroclinic connection between the pure modes (80). This possible heteroclinic orbit will be discussed further below.

3. The third invariant subspace is the intersection of the previous two: $\Sigma_3 = \{|A| = 0, \mathrm{Im}\, B = 0\}$. In other words, this third subspace is the real part of B.

Figure 6 ties together the three invariant subspaces; we see the two pure modes from (80) which lie on the intersection of Σ_3 and the circle of pure modes in $\{|A| = 0\}$ in Σ_1. The heteroclinic connection found with the equations (68) and (69) is sketched in Σ_2.

To employ the analysis and results in [1] and [12], we check that the coefficients of (70) and (71) satisfy

$$e_{12} + e_{21} < 2(e_{11} e_{22})^{1/2}, \text{ and} \tag{83}$$
$$\mu_1 - \mu_2 e_{12} e_{22} - (-\mu_2/e_{22})^{1/2} < 0 < \mu_1 - \mu_2 e_{12} e_{22} + (-\mu_2/e_{22})^{1/2}, \tag{84}$$

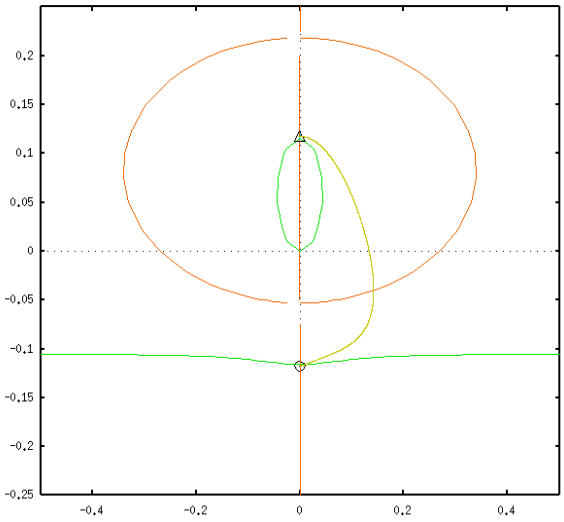

Figure 7: Phase space for Σ_2 with the parameter values of (68)-(69). The curves appearing in all four quadrants are nullclines. The $\triangle$ and $\circ$ mark the pure modes from (80), and there is a heteroclinic orbit pictured between these fixed points. This image was generated using XPPAUT.

in addition to our previous requirements of the signs. These inequalities come from Theorem 3.2 in [1]; in addition, the authors assume further that no mixed modes exist. This assumption is not strictly necessary, but for the equations derived in this project, mixed modes do not appear for a large range of parameter values. With the assumptions (83)-(84), a heteroclinic orbit connecting the points in (80), such as the orbit seen in Figure 7, exists and is structurally stable.

Additionally, we ensure the coefficients satisfy Proposition 5.1 of [1]: if

$$\min\left\{2\mu_2, -\left(\mu_1 - \mu_2 e_{12}/e_{22} - (-\mu_2/e_{22})^{1/2}\right)\right\} > \mu_1 - \mu_2 e_{12}/e_{22} + (-\mu_2/e_{22})^{1/2}, \quad (85)$$

then the heteroclinic orbit is locally asymptotically stable and attracts trajectories in a small enough neighborhood. These trajectories spend long amounts of time near the two pure modes where the dynamics are dominated by the linear terms before passing between the two pure modes in a shorter amount of time. This behavior is illustrated in Figure 8(b): the times in which $|A|$ and $|B|$ are flat are the time periods when the trajectory is close to the two pure modes or transitioning rapidly between them, while the spikes correspond to the times when the trajectory is following closely to the heteroclinic orbit.

Here enters the role of μ and θ from (76): we vary these two parameters as necessary in the first quadrant of the (μ_1, μ_2) plane to find a desirable heteroclinic connection. In general, it is not difficult to satisfy (83)-(85), and there is usually a large neighborhood of μ and θ which yield such a heteroclinic orbit.

Once the heteroclinic orbit is located, it is possible to follow a nearby trajectory using the software package XPPAUT [9]. In addition to plotting the trajectory, this package can simultaneously compute the sizes of $|A|$ and $|B|$ for each time step in the integration. The result of such a computation is seen in Figure 8. When the integration begins near the

pure mode $(0, 0, \sqrt{-\mu_2/e_{22}}, 0)$, the A mode is hardly activated. As t grows, the trajectory moves away from this pure mode, and the A mode is activated. At $t = 114$, $\mathrm{Re}\, B \to 0$; at this t, the size of $|B|$ reaches a minimum that is very small, as the imaginary part of B near the heteroclinic orbit is close to zero. At this point, the size of $|A|$ nearly reaches its maximum. Then as the trajectory nears the second pure mode, $-(0, 0, \sqrt{-\mu_2/e_{22}}, 0)$, the A mode returns to a nearly inactive state while the B mode becomes the driving mode.

This mode switching behavior is expressed physically in terms of the Langmuir cells in Figure 9. At the start and finish of one pass near the heteroclinic orbit, a four-roll state is observed, whereas when the B mode nearly vanishes, a two-roll state is observed. Moreover, after passing along the heteroclinic orbit, the four-roll state is shifted by $W/4$; this shift resembles the behavior observed in the direct numerical simulation of the PDE.

As seen in Figure 8, this process repeats itself as the trajectory loops around and follows near the heteroclinic orbit again. The connection from $-(0, 0, \sqrt{-\mu_2/e_{22}}, 0)$ to $(0, 0, \sqrt{-\mu_2/e_{22}}, 0)$ is related to the translational invariance of the equations, $(A, B) \to (e^{i\vartheta}A, e^{2i\vartheta}B)$ from (22), and thus there is no lateral shifting of the rolls during this phase of the trajectory. Instead, the connection between the pure modes appears in Figure 8 to amount to taking a path in the $\{(x_2, y_1)\}$-plane rotating from the second pure mode to the first one. To calculate this more rigorously, notice that shifting by a fourth of the width of the box, $L = \frac{2\pi}{k_0}$, means a shift of $\frac{\pi}{2k_0}$. Hence

$$A \quad \to \quad e^{\frac{\pi}{2k_0} ik_0} A = e^{\frac{\pi}{2} i} B = iA, \tag{86}$$

$$B \quad \to \quad e^{\frac{\pi}{2k_0} 2ik_0} B = e^{\pi i} B = -B. \tag{87}$$

The $B \to -B$ conversion is simply the switch from the second pure mode to the first one. But after the completion of one pass around the heteroclinic orbit, the real and imaginary parts of A switch via

$$(x_1, y_1) \to i \cdot (x_1, y_1) = (-y_1, x_1). \tag{88}$$

This switch in the real and imaginary parts is illustrated in Figure 10.

Hence the return phase is essentially a reorientation of the manifolds after which the trajectory returns near $(0, 0, \sqrt{-\mu_2/e_{22}}, 0)$ and again follows the heteroclinic clinic orbit in Σ_2. The second trip following the heteroclinic orbit leads to another brief transition to two rolls, followed by a return to a four-roll state with a half-shift (not pictured, but similar to Figure 9).

4 Reduced 3D equations

Up to this point we have restricted attention to the 2D/3C model to examine the rolls in the (y, z)-plane. To visualize the Y junctions, a 3D Lagrangian pattern on the surface, we reintroduce the x-direction into the PDE.

The equations below are not fully 3D; rather, we are performing asymptotic analysis within the framework of the asymptotic analysis of the previous sections, assuming an even longer scale in the downstream direction. We refer to this slow downstream direction as χ. The incompressibility condition on $U = (u, v, w)$ becomes incompressibility in the transverse plane, which we denote by

$$\nabla_\perp U = \partial_y v + \partial_z w = 0.$$

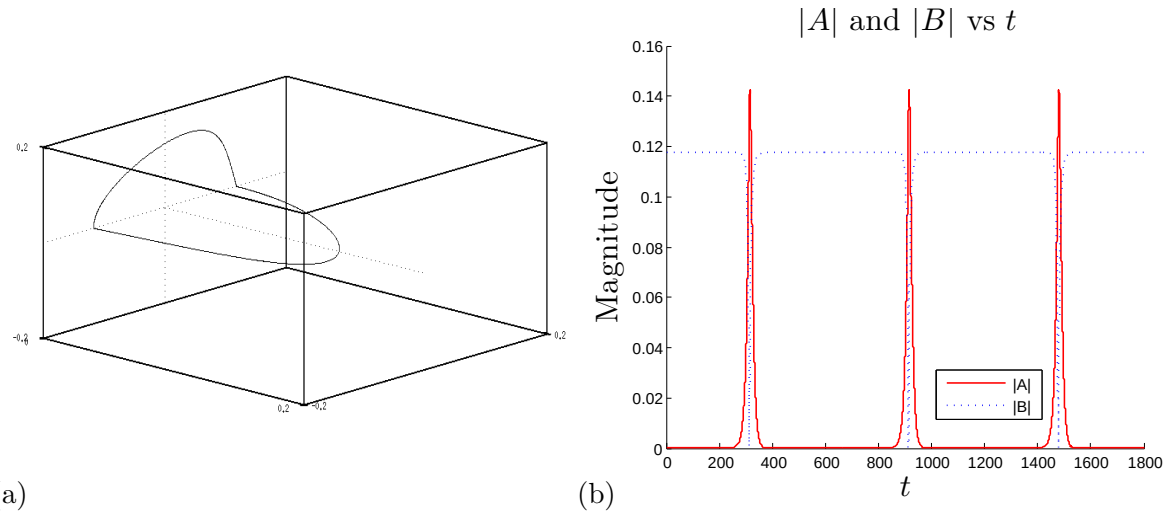

(a) (b)

Figure 8: The subspace shown in (a) is $\{\mathrm{Im}\, B = 0\}$, compare with Figure 5. A trajectory chosen to start near the pure mode $(0, 0, \sqrt{-\mu_2/e_{22}}, 0)$ is pictured. It follows near the heteroclinic orbit of Figure 7 in Σ_2, transitioning between passes along this heteroclinic orbit via the connection that appears vertical. It passes along the heteroclinic orbit approximately three times during the time of integration. This image was created with XPPAUT. The magnitude of the amplitude A for the single mode k_0 compared to the amplitude B for the double mode $2k_0$ for the trajectory in (a) is plotted in (b). At $t = 313$, the magnitude of B reaches its first minimum. The streamfunction at $t = 0$, $t = 313$ and $t = 500$ is plotted in Figure 9.

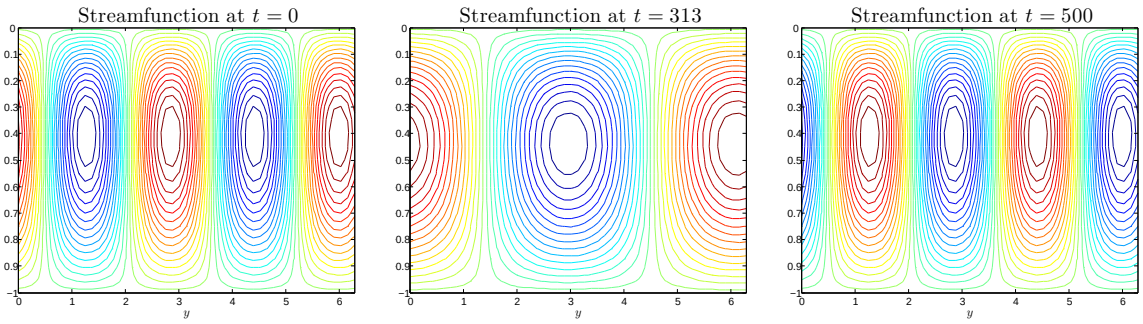

Figure 9: The streamfunction $\psi_1(y, z, t)$ for the trajectory in Figure 8. At the start of the integration ($t = 0$), the orbit is close to the pure mode $(0, 0, \sqrt{-\mu_2/e_{22}}, 0)$, and four rolls are observed. At $t = 313$, when the first minimum of $|B|$ occurs in Figure 8, a two-roll state is observed. At the end of the first loop (around $t = 500$), the orbit has passed near the pure mode $(0, 0, -\sqrt{-\mu_2/e_{22}}, 0)$, and four rolls are again observed, with the predicted shift of half of a period in the y-direction. Repeating this process for all three loops of the orbit continues this pattern.

Hence the streamfunction ψ is still defined in this 3D context.

Following the derivation in Chini *et al.* [3] with their downstream variable X, the coordinate version of the PDE with slow advection in the downstream direction is

$$\begin{aligned}
\partial_t U + J(U, \psi) - \partial_y \psi &= -\partial_X \Pi + La \nabla_\perp^2 U, && (89)\\
\partial_t \Omega + J(\Omega, \psi) + U_s(z)\partial_X \Omega &= U_s'(z)(\partial_X \partial_z \psi - \partial_y U) + La \nabla_\perp^2 \Omega, && (90)\\
\nabla_\perp^2 \Pi &= 2J(\partial_y \psi, \partial_z \psi) + \nabla_\perp \cdot (U_s(z) \nabla_\perp u)\,, && (91)\\
&\quad + U_s'(z)\partial_X \partial_y \psi, && (92)\\
\nabla_\perp^2 \psi &= -\Omega. && (93)
\end{aligned}$$

Unlike in [3], we will assume mixed boundary conditions on u and exponential Stokes drift, as well as different boundary conditions on the pressure as a result of these adjustments.

4.1 Linear analysis

In Section 2, taking the curl of the equations caused the pressure terms to vanish. In this reduced 3D setting, it does not. Hence in addition to the base state $U_B(z)$ in the x-direction from before, we will also linearize about the pressure base state $\Pi_B(z)$. The perturbation terms are $u_p(X, y, z, t)$, $\psi(X, y, z, t)$, $p(X, y, z, t)$ and $\Omega(X, y, z, t)$, and the total fields are written

$$\begin{aligned}
u(X, y, z, t) &= U_B(z) + u_p(X, y, z, t), && (94)\\
\psi(X, y, z, t) &= \psi(X, y, z, t), && (95)\\
\Pi(X, y, z, t) &= \Pi_B(z) + p(X, y, z, t), && (96)\\
\Omega(X, y, z, t) &= \Omega(X, y, z, t). && (97)
\end{aligned}$$

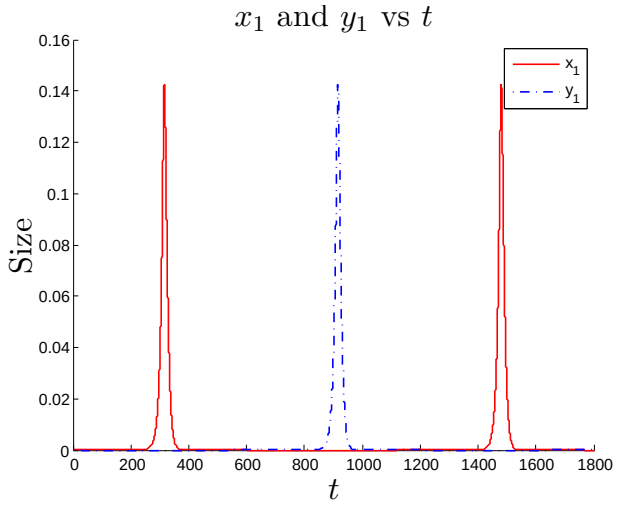

Figure 10: The three trips of the orbit from Figure 8(a) are pictured in terms of the real and imaginary parts of $A(\tau)$, see equation (88).

In addition to the previous boundary conditions on u, Ω and ψ, we note that the boundary condition on the pressure is $\partial_z p = 0$ along $z = 0$ and $\partial_z p = U_s(-1) \cdot \gamma\, u_p$ along $z = -1$. Linearizing about the base state yields

$$\begin{aligned}
\partial_t u - \partial_y \psi &= -\partial_X p + La\nabla_\perp^2 u, && (98)\\
\partial_t \Omega + U_s(z)\partial_X \Omega &= U_s'(z)(\partial_X \partial_z \psi - \partial_y u) + La\nabla_\perp^2 \Omega, && (99)\\
\nabla_\perp^2 p &= \nabla_\perp \cdot (U_s(z)\nabla_\perp u) + U_s'(z)\partial_X \partial_y \psi, && (100)\\
\nabla_\perp^2 \psi &= -\Omega. && (101)
\end{aligned}$$

To reduce from four equations to three, we use the definition of the vorticity Ω in (101) to write

$$\begin{aligned}
\partial_t u - \partial_y \psi &= -\partial_X p + La\nabla_\perp^2 u, && (102)\\
-\partial_t \nabla_\perp^2 \psi - U_s(z)\partial_X \nabla_\perp^2 \psi &= U_s'(z)(\partial_X \partial_z \psi - \partial_y u) - La\nabla_\perp^4 \psi, && (103)\\
\nabla_\perp^2 p &= \nabla_\perp \cdot (U_s(z)\nabla_\perp u) + U_s'(z)\partial_X \partial_y \psi. && (104)
\end{aligned}$$

We again make a normal mode ansatz. In this case, there is an additional term for the downstream direction with wavenumber ℓ, resulting in

$$\begin{pmatrix} u \\ \psi \\ p \end{pmatrix} = \begin{pmatrix} \hat{u}(z) \\ \hat{\psi}(z) \\ \hat{p}(z) \end{pmatrix} e^{iky} e^{\sigma t} e^{i\ell X}, \qquad (105)$$

where $\hat{u}(z)$, $\hat{\psi}(z)$ and $\hat{p}(z)$ are the structures in the vertical direction. Let $D = \frac{\partial}{\partial z}$ as before, then with the ansatz, (102)-(103) can be written as an eigenvalue problem

$$\begin{aligned}
\sigma u &= La(D^2 - k^2)u + ik\psi - i\ell p, && (106)\\
0 &= -\left[U_s(z)(D^2 - k^2) + U_s'(z)D\right] u + U_s'(z)k\ell\psi + (D^2 - k^2)p, && (107)\\
\sigma(D^2 - k^2)\psi &= ikU_s'(z)u + \left[La(D^2 - k^2)^2 - i\ell U_s(z)(D^2 - k^2) - i\ell U_s'(z)D\right]\psi, && (108)
\end{aligned}$$

with eigenvalue σ. Repeating the steps of Section 3.1, in matrix form this is

$$A \begin{pmatrix} u \\ \psi \\ p \end{pmatrix} = \sigma B \begin{pmatrix} u \\ \psi \\ p \end{pmatrix},$$

where

$$A = \begin{pmatrix} La(D^2-k^2) & ik & -i\ell \\ ikU_s'(z) & La(D^2-k^2)^2 - i\ell U_s(z)(D^2-k^2) - i\ell U_s'(z)D & 0 \\ -\left[U_s(z)(D^2-k^2) + U_s'(z)D\right] & U_s'(z)k\ell & (D^2-k^2) \end{pmatrix}$$

and

$$B = \begin{pmatrix} 1 & 0 & 0 \\ 0 & D^2-k^2 & 0 \\ 0 & 0 & 0 \end{pmatrix}.$$

We set $\det(A - \sigma B) = 0$ to find the dispersion relation numerically, as in the 2D/3C case. In this setting, the horizontal wavenumber k for the single mode is fixed at the value of k_0 computed for the same parameters in the 2D/3C setting. Similarly, the wavenumber is $2k_0$ for the double mode, and the forcing term La is fixed at La_0.

Once these assignments are made, the growth rate σ becomes of function of ℓ. Computing σ using the same pseudospectral approach as before, we can individually find the real and imaginary parts of σ as functions of ℓ, see Figure 11. The real part of the growth rate is quadratic while the imaginary part is linear; this can be verified by plotting the first and second derivatives of the curves.

Setting the slow variable χ to be $\chi = \varepsilon X$ with ε as before, the equation for the growth rate σ_1 for A becomes

$$\sigma_1 = \mu_1 - i\ell v_{g_1} - \nu_1 \ell^2, \tag{109}$$

while for B it is

$$\sigma_2 = \mu_2 - i\ell v_{g_2} - \nu_2 \ell^2, \tag{110}$$

where v_{g_j}, $j = 1, 2$, denotes the group velocity for the wavepacket. The coefficients are computed numerically; for the parameter set used for (68)-(69), the growth rates are

$$\sigma_1 = \mu_1 - 0.1548i\ell - 0.0521\ell^2, \tag{111}$$

and

$$\sigma_2 = \mu_2 - 0.1666i\ell - 0.0397\ell^2. \tag{112}$$

In Fourier space, we interpret these equations in terms of the ansatz. In physical space, we set $i\ell = \partial_\chi$ and $-\ell^2 = \partial_{\chi\chi}$. Hence to the ODEs we append the slow χ derivatives to obtain a set of reduced PDEs for $A(t, \chi)$ and $B(t, \chi)$:

$$A_t = \mu_1 A - 0.0801\overline{A}B - 0.0758|A|^2 A - 0.3867|B|^2 A - 0.1548A_\chi + 0.0521A_{\chi\chi}, \tag{113}$$

$$B_t = \mu_2 B + 0.0987A^2 - 0.7563|A|^2 B - 0.3334|B|^2 B - 0.0833B_\chi + 0.0099B_{\chi\chi}. \tag{114}$$

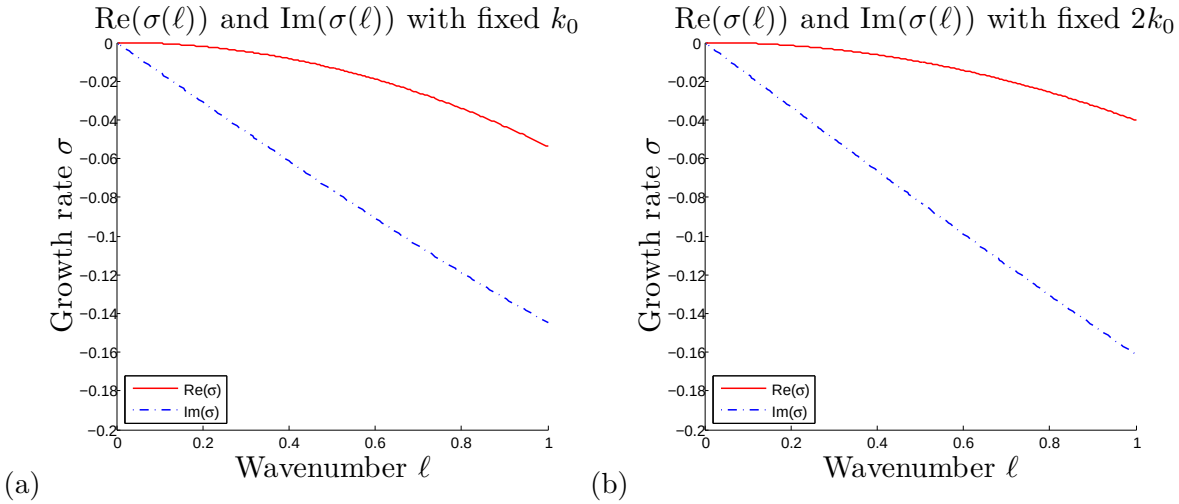

Figure 11: Each plot shows the real and imaginary parts of σ as a function of the downstream wavenumber ℓ, as computed in Section 4.1; (a) is for the k_0 mode, and (b) is for the $2k_0$ mode. The real part of each is quadratic, while the imaginary part is linear.

5 Conclusion

With a 2D/3C model, we performed a center manifold reduction to derive evolution equations for the amplitudes A for the mode e^{ik_0y} and B for the mode e^{2ik_0y}. Using Matlab, for an extensive range of parameters values we were able to numerically compute coefficients that satisfy certain inequalities guaranteeing the existence of a robust and attracting heteroclinic orbit in an invariant subspace of the center manifold. Numerical simulations of trajectories close to this orbit reveal a switching behavior between a 2-roll state and a 4-roll state consistent with the behavior observed in direct numerical simulations of the governing PDE. The dynamics explored in this paper assumed an idealized state; for analysis of structurally stable heteroclinic cycles in a system with $O(2)$ symmetry with additive noise, we refer to work by Stone and Holmes. In [14], they find that such white noise does not drastically affect the solutions in the phase space of the evolution equations, but rather leads to a particular selection of timescales.

Lastly, we used a set of reduced 3D equations to introduce slow advection in the downstream direction to convert the ODEs to PDEs. A future goal is to derive the PDE for the zero mode to get the drift effect and show how simulating these PDEs will exhibit the Lagrangian Y junction patterns observed on the surface of the ocean. We will also derive a set of equations for A, B and C which couple A and B to C. This coupling will be used to examine how the dynamics of the A and B modes are affected by downstream advection.

6 Acknowledgements

I am very grateful to the Woods Hole Oceanographic Institution and to many individuals for this summer. In addition to thanking my three advisors Edgar Knobloch, Greg Chini and Keith Julien, I would also like to thank Geoffrey Vasil of the University of Toronto for several meaningful conversations in July. I enjoyed sharing this experience with all of the other fellows; in particular, I would like to thank Rosie Oglethorpe, Felicity Graham, Alban Sauret, and Cédric Beaume for useful discussions on my project. Lastly, I appreciated the atmosphere created by all the visitors and faculty and would like to acknowledge Colm-cille Caulfield and Charlie Doering for their direction this summer.

References

[1] Armbruster, Dieter, John Guckenheimer, and Philip Holmes. Heteroclinic cycles and modulated travelling waves in systems with $O(2)$ symmetry. *Physica 29D*, 257-282 (1988).

[2] Bhaskaran, Rajesh and Sidney Leibovich. Eulerian and Lagrangian Langmuir circulation patterns. *Physics of Fluids*, 14, 2557 (2002).

[3] Chini, Gregory P., Keith Julien and Edgar Knobloch. An asymptotically reduced model of turbulent Langmuir circulation. *Geophysical & Astrophysical Fluid Dynamics*, 103: 2,179-197 (2009).

[4] Chossat, P. The bifurcation of heteroclinic cycles in systems of hydrodynamical type. *Dynam. Cont. Discr. Impuls. Syst.* 8, 575 (2001).

[5] Cox, Stephen M. and Sidney Leibovich. Langmuir circulations in a surface layer bounded by a strong thermocline. *Journal of Physical Oceanography* Vol. 23, pp. 1300-1345 (1992).

[6] ———. Large-scale Langmuir circulation and double-diffusive convection: evolution equations and flow transitions. *J. Fluid Mech.* Vol. 276, pp. 189-210 (1994).

[7] ———. Large-scale three-dimensional Langmuir circulation. *Physics of Fluids* 9, 2851 (1997).

[8] Craik, A.D.D. and S. Leibovich. A rational model for Langmuir circulations. *J. Fluid Mech.*, Vol. 73, pp. 401-426 (1976).

[9] Ermentrout, B. Dynamical systems software with continuation and bifurcation capabilities (1999), available via FTP from directory/pub/bardware at ftp.math.pit.edu.

[10] Krupa, Martin and Ian Melbourne. Nonasymptotically stable attractors in $O(2)$ mode interactions. From *Normal Forms and Homoclinic Chaos*, editors William F. Langford and Wayne Nagata. AMS (1995).

[11] Mercader, I., J. Prat and E. Knobloch. The 1:2 mode interaction in Rayleigh-Benard convection with weakly broken midplane symmetry. *Int. J. Bif. Chaos.* 11: 27-41 (2001).

[12] Porter, J. and E. Knobloch. New type of complex dynamics in the 1 : 2 spatial resonance. *Physica D*, 159, 125-154 (2001).

[13] Proctor, M.R.E. and C.A. Jones. The interaction of two spatially resonant patterns in thermal convection. Part 1. Exact 2:1 resonance. *J. Fluid Mech.* Vol. 188, pp. 301-335 (1988).

[14] Stone, Emily and Philip Holmes. Random Perturbations of Heteroclinic Attractors. *SIAM J. Appl. Math.* 50(3), 726âĂŞ743.

[15] Thorpe, S.A.. Langmuir circulation. *Annu. Rev. Fluid Mech.* 36: 55-79 (2004).

[16] Trefethen, Lloyd N. *Spectral Methods in Matlab*. SIAM (2000).